Check for updates

Foster Lauren (Orcid ID: 0000-0003-0762-3393)

Author Manuscript

Sensitivity analysis of hydraulic conductivity and Manning's *n* parameters lead to new method to scale effective hydraulic conductivity across model resolutions.

Authors: Lauren Foster[1*], Reed Maxwell[1]

[1]Colorado School of Mines
*Corresponding Author
lfoster@mines.edu

Running Title: Scaling effective hydraulic conductivity
Keywords: Hydraulic Conductivity, Manning's n, Resolution, Integrated Modeling, Scaling, Parameter Estimation

This is the author manuscript accepted for publication and has undergone full peer review but has not been through the copyediting, typesetting, pagination and proofreading process, which may lead to differences between this version and the Version of Record. Please cite this article as doi: 10.1002/hyp.13327

This article is protected by copyright. All rights reserved.

10991085, 2019, 3, Downloaded from https://onlinelibrary.wiley.com/doi/10.1002/hyp.13327, Wiley Online Library on [23/01/2023]. See the Terms and Conditions (https://onlinelibrary.wiley.com/terms-and-conditions) on Wiley Online Library for rules of use; OA articles are governed by the applicable Creative Commons License

Author Manuscript

10991085, 2019, 3, Downloaded from https://onlinelibrary.wiley.com/doi/10.1002/hyp.13327, Wiley Online Library on [23/01/2023]. See the Terms and Conditions (https://onlinelibrary.wiley.com/terms-and-conditions) on Wiley Online Library for rules of use; OA articles are governed by the applicable Creative Commons License

This article is protected by copyright. All rights reserved.

Author Manuscript

10991085, 2019, 3, Downloaded from https://onlinelibrary.wiley.com/doi/10.1002/hyp.13327, Wiley Online Library on [23/01/2023]. See the Terms and Conditions (https://onlinelibrary.wiley.com/terms-and-conditions) on Wiley Online Library for rules of use; OA articles are governed by the applicable Creative Commons License

Abstract

Hydrological modeling is an important tool for research, policy, and management, but uncertainty remains about parameters transferability from field observations made at small scale to models at the catchment scale and larger. This uncertainty compels the need to develop parameter relationships that are translatable across scale. In this study we compare the changes to modeled processes as resolution is coarsened from 100m to 1km in a topographically-complex, 255km^2 Colorado River headwater catchment. We conducted a sensitivity analysis for hydraulic conductivity (*K*) and Manning's *n* parameters across 4 orders of magnitude. Results showed that *K* acts as a moderator between surface and subsurface contributions to streamflow, while *n* moderates the duration of high intensity, infiltration-excess flow. The parametric sensitivity analysis informed development of a new method to scale effective hydraulic conductivity across modeling resolutions in order to compensate for the loss of topographic gradients as resolution is coarsened. A similar mathematical relationship between *n* and lateral resolution changes was not found, possibly because *n* is also sensitive to time discretization. This research provides an approach to translate hydraulic conductivity parameters from a calibrated coarse model to higher resolutions where the number of simulations are limited by computational demand.

1. Introduction

Alpine, snowmelt-dominated catchments are the source of water for more than 1/6th of the world's population (Barnett *et al.*, 2005). In the United States, snowpack in the Rocky Mountains provides more than 85% of the streamflow for the Upper Colorado River Basin (Ikeda *et al.*, 2010), which in turn provides water supplies to major cities and farming communities from Colorado to California. These catchments are topographically complex, leading to nonlinear relationships between water and energy fluxes that can be difficult to capture with statistical or conceptual models (Beniston, 2003; Wood *et al.*, 2004). The nascent impacts of regional warming will complicate these nonlinearities; a recent review of elevation-dependent warming studies demonstrated consensus in the literature that mountain regions are more sensitive to increasing temperatures, in most cases making them drier and more arid (Pepin *et al.*, 2015). Changing climate exacerbates the challenges of modeling these systems by calling into question the ability of stationary models, which are informed by historical datasets, to be applicable in future conditions.

These factors are all major reasons that high-resolution, integrated models have been proposed as a useful tool to better understand mountain regions, especially in a future climate. Physically-based models are built from theoretical equations of water fluxes measured and studied either in a lab or in small plots. These models are being applied over increasingly larger extents and higher resolutions as the need to model full catchments, multiple catchments, or even entire

This article is protected by copyright. All rights reserved.

continents has become a community research goal (Wood *et al.*, 2011b; Bierkens *et al.*, 2015; Maxwell and Condon, 2016). Hyper-resolution integrated models have been the focus of much new research, often because they have capabilities to propagate nonlinear relationships through a complex system like the Rocky Mountains. However, there remain many challenges to achieving a realistic representation of complex systems at many scales.

In response to the Wood *et al* 2011b call for hyper-resolution models, Beven and Cloke 2012 argued that scale-dependent representations need to be considered more explicitly before models can be pushed to higher resolutions or larger extents. This need to better describe scale dependency has also been highlighted in previous modeling studies as the aggregation of topography at different lateral resolutions has been shown to impact the water balance (Zhang and Montgomery, 1994; Niedda, 2004; Vivoni *et al.*, 2005; Bormann, 2006; Giertz *et al.*, 2006; Dixon and Earls, 2009; Sciuto and Diekkrüger, 2010; Sulis *et al.*, 2011; Jana and Mohanty, 2012). There have been efforts to explore model sensitivity to variability in resolution, and resulting process representation, for land surface variables, subsurface variables, and through sensitivity studies (Srivastava *et al.*, 2014; Jefferson *et al.*, 2015a; Shrestha *et al.*, 2015; Gilbert *et al.*, 2016; Markovich *et al.*, 2016). While these results have been tested in specific individual domains, physically-based models still need further experiments to test conceptual models of the subsurface (Ala-aho *et al.*, 2017) and how these parameters affect the scaling of mathematical representations as resolution is coarsened beyond the lab or plot where the relationships were determined (von Gunten *et al.*, 2014).

Streamflow, subsurface flow, and even evapotranspiration have been shown to be sensitive to parameterization of hydraulic conductivity (K) or permeability (k) (Srivastava *et al.*, 2014). At the same time, measurement of K at different scales is uncertain. While hydraulic conductivity (K) can be measured in controlled laboratory experiments, effective K, the aggregated value of K at larger extents, changes with scale (Brace, 1980; Clauser, 1992; Gelhar *et al.*, 1992; Niedda, 2004). Crystalline rocks that underlie many mountain chains, such as the site studied here, have been shown to vary up to 8 orders of magnitude in laboratory tests and regional averages (Freeze, R.A., Cherry, 1979; Domenico and Schwartz, 1997; Welch and Allen, 2014). Numerous studies have examined the scaling of K, especially in the contaminant transport community (Sudicky and Huyakorn, 1991; Zheng and Gorelick, 2003), but rarely has this scaling behavior been contextualized in terms of catchment and larger modeling efforts. While advances in hydrogeophysics have increased the potential to map K at larger scales, there remains significant uncertainty in these estimates (Robinson *et al.*, 2015).

Despite the coincidence of parameter sensitivity and measurement uncertainty, limited research has explored model sensitivity to K parameterization and spatial scale in real domains. In one such study, Kurylyk and Hayashi 2017 used an integrated, 2D hillslope model to diagnose diurnal streamflow signals during snowmelt periods. By exploring model sensitivity to

This article is protected by copyright. All rights reserved.

Author Manuscript

10991085, 2019, 3, Downloaded from https://onlinelibrary.wiley.com/doi/10.1002/hyp.13327, Wiley Online Library on [23/01/2023]. See the Terms and Conditions (https://onlinelibrary.wiley.com/terms-and-conditions) on Wiley Online Library for rules of use; OA articles are governed by the applicable Creative Commons License

Author Manuscript

subsurface layer parameterization, they found that upper *K* layer controlled the lag in diurnal signal, while lower layer *K* controlled the signal damping. Their innovative methods could be applied to better parameterize *K* in models of data-poor mountain regions, and integrated studies like this are needed at catchment and larger scales. Niedda 2004 used information content and entropy formulations to improve the parameterization of K across modeling resolutions. The author demonstrates a quantifiable relationship between topographic gradients and effective K with a model that routes surface flow and solves for 2D subsurface flow using a simplified realization of K decreasing with depth. They describe the need to extend their research to modeling applications with more detail both in catchment representation and in modeled processes. These studies highlight the need to go beyond idealized domains and test integrated model parameterization in real-world systems.

Here, we present a suite of sensitivity analyses for two sensitive parameters to modeling flow– hydraulic conductivity (*K*) and Manning's *n*– compared at two modeling resolutions– 1km and 100m, in a 255km^2 Rocky Mountain catchment. These results systematically document changes in physical modeling behavior as *K* and *n* are varied over 4 orders of magnitude in a real, complex, and heterogeneous mountain system. Further, by using effective values that incorporate grid scale driven differences in topography, we develop a procedure for downscaling or upscaling hydraulic conductivity to higher or lower lateral resolutions, which we test across four resolutions. A similar scaling relationship for *n* was not found, possibly due to higher sensitivity to time discretizations than lateral resolution, and possibly because a similar relationship does not exist for the empirical formulation of Mannings' *n*. Given that a traditional calibration of numerically large model applications demands extensive computational resources, this study provides tools for future model developers to choose appropriate parameters for their domain, taking into account changes to physical process representation as resolution is coarsened to cover larger areas (or more finely discretized to approach a hyper-resolution system). This methodology can be used to reduce computational demand while choosing appropriate parameters for large-scale, integrated modeling efforts.

2. Methods

In order to understand how processes scale in a modeling environment, we conducted a parametric sensitivity analysis at two different grid resolutions: 100m and 1km (Section 2.3). Though this experiment could be conducted in any region with any physically-based model, here we present results using the integrated model ParFlow-CLM (Section 2.1) in the East River Basin, Colorado. As is typical for alpine regions, there are limitations to the available data, both for meteorological input and validation. We discuss the study area and available data used to inform and drive the integrated model in Section 2.2.

This article is protected by copyright. All rights reserved.

10991085, 2019, 3, Downloaded from https://onlinelibrary.wiley.com/doi/10.1002/hyp.13327, Wiley Online Library on [23/01/2023]. See the Terms and Conditions (https://onlinelibrary.wiley.com/terms-and-conditions) on Wiley Online Library for rules of use; OA articles are governed by the applicable Creative Commons License

Author Manuscript

10991085, 2019, 3, Downloaded from https://onlinelibrary.wiley.com/doi/10.1002/hyp.13327, Wiley Online Library on [23/01/2023]. See the Terms and Conditions (https://onlinelibrary.wiley.com/terms-and-conditions) on Wiley Online Library for rules of use; OA articles are governed by the applicable Creative Commons License

2.1 Model

We use the integrated hydrologic model ParFlow (PF) coupled to the Common Land Model (CLM). PF simultaneously solves the 3D Richards equation and shallow water equations to determine a pressure head in every cell (Kollet and Maxwell, 2006; Maxwell, 2013). CLM solves the surface energy budget, explicitly representing evaporation, transpiration, snow processes, heat fluxes, and radiation partitioning (Jefferson and Maxwell, 2015; Jefferson *et al.*, 2015b; Ferguson *et al.*, 2016). CLM and PF are connected across four subsurface layers to represent rooting depths and lateral water transfer in the variably saturated subsurface (Maxwell and Miller, 2005). While there are many parameters included in the fully-coupled model, hydraulic conductivity (*K*) and Manning's *n* are some of the most important to representing flow accurately as discussed below.

In simple language, water flows downhill due to the force of gravity and is resisted by frictional forces. This relationship is defined by the Darcy flux (Equation 1) in the subsurface. In equation 1 saturated hydraulic conductivity, $\mathbf{K}_s(x)$, and relative permeability, $K_r(h)$, combine to form the measured hydraulic conductivity (*K*) we discuss in this paper, which is the inverse of the frictional force resisting downhill flow. The head gradient is defined by pressure head and elevation, $\nabla(h + z)$. Together, these two terms determine the volume and rate of flow in the subsurface.

EQUATION 1:

$$\mathbf{q} = \phi S_w(h)\mathbf{v} = -\mathbf{K}_s(x)k_r(h)\nabla(h + z)$$

$\mathbf{q}$: Darcy flux (m hr^{-1})
ϕ: Porosity in the cell (-)
S_w: Relative saturation (-)
h: Pressure head (m)
$\mathbf{v}$: Subsurface flow velocity (m hr^{-1})
$\mathbf{K}_s(x)$: Saturated hydraulic conductivity tensor (m hr^{-1})
$K_r(h)$: Relative permeability (-)
z: Elevation (m)

In PF, the orthogonal grid is transformed to mimic the slope of the underlying topography, and Equation 1 becomes Equation 2 (expanded in Equation 3). For a full derivation of Darcy flow represented by a terrain-following-grid, see Maxwell 2013.

EQUATION 2:

$$\mathbf{q} = -\mathbf{K}_s(x)k_r(h)\,[\nabla(h + z)cos\theta + sin\theta]$$

EQUATION 3:

$$\mathbf{q} = -\mathbf{K}_s(x)k_r(h)\nabla(h + z)cos\theta + sin\theta(-\mathbf{K}_s(x)k_r(h))$$

This article is protected by copyright. All rights reserved.

θ: Local angle of slope (-)
All other terms defined below Equation 1

Surface flow is similarly determined by gravity and friction, and here we calculate flow from pressure head using Manning's equation (Equation 4). Put simply, surface flow increases with a higher gravity term (determined by the slope and head terms in Manning's equation). Manning's *n* represents friction on the surface, so as *n* increases flow decreases.

EQUATION 4:

$$Q = \frac{\Delta y \cdot h}{n}(h^{\frac{2}{3}} \cdot \sqrt{S})$$

Q: Discharge (m^3hr^{-1}), calculated at the outlet cell for a watershed in the domain
Δy: Cell width (m), model analog for channel width
n: The Gauckler-Manning coefficient ($hr\ m^{-1/3}$)
h: Pressure head at the outlet cell (m)
S: Slope of the hydraulic grade line at the outlet cell (-)

Streamflow is a complex, integrated signal that includes the impact of many factors like landcover, geology, climate, and topography. However, the basic mathematics of these flow calculations highlight the importance of *K* and *n* parameters to streamflow simulation.

2.1 Site Description

The East River catchment is a $255km^2$ basin northeast of Crested Butte, Colorado USA (Figure 1). The basin contains four major ecosystems- alpine, subalpine, montane, and riparian. Geology in the basin is dominated by low-conductivity crystalline formations and the more erodible Mancos shale formation, but the east side also contains steeply dipping sedimentary beds. The climate is continental subarctic- precipitation generally falls as snow from October to March, monsoon rainfall occurs in the late summer months, and temperatures are cold through the winter and cool in the summer– mean temperatures at the mid-elevation station are -8.3°C in December and 11°C in June. With about 0.8m of precipitation each year (1985-2014 average), steep topography leading to steep temperature and humidity gradients, heterogeneous landcover and complex geology, it is considered representative of most headwater basins in the western Rocky Mountains that feed the Colorado River (Battaglin *et al.*, 2012). Additional site details can be found in McCabe and Hay, 1995; Winnick *et al.*, 2017; Carroll *et al.*, 2018.

2.2.1 Observed Meteorology

This article is protected by copyright. All rights reserved.

Author Manuscript

10991085, 2019, 3, Downloaded from https://onlinelibrary.wiley.com/doi/10.1002/hyp.13327, Wiley Online Library on [23/01/2023]. See the Terms and Conditions (https://onlinelibrary.wiley.com/terms-and-conditions) on Wiley Online Library for rules of use; OA articles are governed by the applicable Creative Commons License

Author Manuscript

10991085, 2019, 3, Downloaded from https://onlinelibrary.wiley.com/doi/10.1002/hyp.13327, Wiley Online Library on [23/01/2023]. See the Terms and Conditions (https://onlinelibrary.wiley.com/terms-and-conditions) on Wiley Online Library for rules of use; OA articles are governed by the applicable Creative Commons License

The models are driven by hourly observed meteorology developed from the best combination of available products. Water year 2006 most closely represented historical means for the region (1985-2014) and was therefore chosen as the simulation period. There are two SNOTEL stations within the domain and one EPA Castnet site located at the base of the valley in Gothic, CO (Figure 1). An analysis of weather stations within 50km of the model domain showed that a temperature inversion in which low elevation locations were colder than mid-elevations was present from Oct-May, but not in the summer months (Jun, Jul, and Aug). The Butte station was chosen for the hourly variability of temperature because it was at an intermediate elevation (3097m). A dry adiabatic lapse rate was then used to minimize error relative to temperature records at the high elevation Schofield station (3261m). For summer months this lapse rate was used to determine temperature in every cell based on elevation. During inversion months a separate lapse rate was fit between Butte and Castnet, the lowest station (2915m). The loss of almost 200m of elevation relief between the 100m and 1km models necessitated different lapse rate calculations for the 1km model such that both models accurately represented temperature records where observations were available. Despite these unique lapse rates there is less than 1°C difference in average temperature forcing between the 1km and 100m models.

Precipitation input to the model is provided from the National Land Data Assimilation System (NLDAS-2) (Cosgrove, 2003; Mitchell, 2004). Given that there are only 3 stations within the domain, a bilinear interpolation of the NLDAS-2 precipitation dataset offers the best heterogeneity despite being limited by resolution– with only 4 pixels falling in the model domain. This coarse resolution for precipitation input has two main impacts. First, high elevation snowpack is underestimated, likely because of the averaging that occurs in the NLDAS-2 product. Second, summer storms initialize and dissipate much more quickly than is realistic because precipitation heterogeneity is not represented. The 2006 water year underestimates SWE at the lower elevation Butte station, but a 1km run over multiple years shows that this is not a consistent low bias in precipitation (Figure 2).

NLDAS-2 datasets were also used for windspeed and humidity, as they were the only product available across the entire domain. A downscaled NLDAS-2 product developed by Princeton was used for short and longwave radiation (Pan *et al.*, 2016). Finally, pressure was calculated in every cell using the spatially heterogeneous temperature and humidity datasets.

2.2.2 Streamflow Observations

There are four pressure transducers with data from WY2006– Gothic Creek, Rustlers Creek, Copper Creek, and the East River just below the confluence with Copper (Peckarsky *et al.*, 2014). These gauges and their respective upstream areas are shown in Figure 1. It should be noted that the East River subcatchment includes all three of the smaller basins but does not

This article is protected by copyright. All rights reserved.

include the entire model domain. Estimates of daily streamflow were produced based on these observations.

These observed streamflow data suffered from artifacts and inaccuracy (red portions in Figure 4) that resulted from measurement error, e.g. pressure transducers emplaced under frozen streams. The baseflow period in Rustlers shows a spike in pressure that is likely an error in the transducer, and the baseflow period in the East River is close to 0; however, this gauge is immediately downstream of the Copper gauge which shows a higher baseflow recession, indicating there must have been some malfunction with both the East and Gothic gauges. Despite the errors and missing points in the data, the total volumes of the peak flow and summer flows were accurately recorded. Observed streamflow is consistent with headwater basins, with low baseflow volumes, a strong peak flow period coinciding with snowmelt, and flashy summer flows responding to summer monsoon rain events (Figure 4).

2.3.1 Sensitivity Analysis

Two models of the East River Basin were constructed at 1km and 100m resolution; inputs are shown in Figure 3. Landcover was defined from the 30m National Land Cover Database based on highest prevalence per model cell, and corresponding Manning's *n* were assigned according to empirical values (Brutsaert, 2008). Below the land surface there are 5 subsurface model layers. The thickness of the model is uniform laterally, with no defined 'inactive' cells. For further explanation of a terrain-following-grid please see Maxwell 2013. The top three layers, at 0.1, 0.3, and 0.6m depths respectively, are soil layers. Three soil layers allows more definition in soil water content throughout the root zone. Soils were defined from the SSURGO database, then corrected based on landcover and geologic maps to include exposed geology from the geology layer. The 8m geology layer was defined with USGS maps and augmented by local knowledge of the basin (Williams, 2017). The discretization of soil vs. geology was chosen based on estimates of soil depths in the catchment and is consistent with the standard Noah land surface model implementation (Chen and Dudhia, 2001). Below the geology layer is a homogenous 21m layer representing fractured bedrock. Hydraulic conductivity values were defined from lithologic permeability values obtained from a combination of USGS maps, Maxwell *et al* 2015, and Gleeson *et al* 2011. The inputs were defined for the 100m, high resolution model, and then aggregated to a 1km scale using the mean (slopes) and the mode (geology, soil, landcover). The tables in Figure 3 list the small changes to landcover and geologic composition between the 1km and 100m model due to aggregation. One of the primary effects from resolution coarsening is a decrease in the range of elevation by 190m.

A parametric sensitivity analysis was designed to test model sensitivity to changes in hydraulic conductivity (*K*) and Manning's (*n*). Cases varying specific storage were also run, but their impacts to flow were negligible compared to Manning's *n* and *K* so they are not presented here.

Author Manuscript

This article is protected by copyright. All rights reserved.

10991085, 2019, 3, Downloaded from https://onlinelibrary.wiley.com/doi/10.1002/hyp.13327, Wiley Online Library on [23/01/2023]. See the Terms and Conditions (https://onlinelibrary.wiley.com/terms-and-conditions) on Wiley Online Library for rules of use; OA articles are governed by the applicable Creative Commons License

Author Manuscript

The sensitivity analysis discussion will be confined to the 18 modeling runs presented in Table 1. *K* was modified in each of the layers shown in Figure 3 by scaling original estimates by orders of magnitude below and above initial estimates. Manning's *n* was modified both in magnitude and by spatial distribution patterns. Magnitude was varied from a minimum of the empirical values (0.02 $s/m^{1/3}$) up to four orders of magnitude above the minimum (20 $s/m^{1/3}$). Three spatial distributions of *n* were compared: (1) constant *n* everywhere, (2) *n* determined by the baseline vegetation and then scaled, and (3) with the stream cells defined and assigned a typical stream Manning's (0.035 $s/m^{1/3}$) and all other cells determined by vegetation.

2.3.2 Computational Demand

Each of the 18 model configurations shown in Table 1 were applied to the 1km and 100m resolution models, for a total of 36 simulations. All the models were forced with WY2006 data repeatedly until reaching a dynamic equilibrium, where the total change in storage over the year was less than 1% of the precipitation entering the domain in WY2006.

The 100m model configurations were run on 64 processors and required approximately 14 hours of simulation time per water year. Each configuration required an average of 3 years to reach dynamic equilibrium, and the baseline case required 5. Thus the total computational demand for the 100m sensitivity experiments shown here was approximately 50,000 core hours. Given the number of hours required to do these 18 model runs, a traditional parameter estimation experiment, which requires 10's to 100's of model runs per parameter, would not be feasible. Here the parametric sensitivity analysis replaces a traditional parameter estimation process. We study changes in flow resulting from *K* and *n* parameter value sweeps, and then develop a process-based method for scaling these parameters as resolution changes. Ultimately, a methodology like this could inform model building by upscaling measured values to appropriate parameter choices at different modeling resolutions.

3. Results and Discussion

3.1 Hydraulic conductivity sensitivity

Figure 4 shows observed and simulated flow from the baseline parameter sets. Though the composition of landcover and geology are similar between the 1km and 100m models (Figure 1), these same parameters have a dramatically different impact on flow at different modeling resolutions (Figure 4).

The 1km model represents the first peak of snowmelt well, but underestimates the second peak. We attribute this result to the low-bias in high-elevation snowpack in the NLDAS-2 precipitation

This article is protected by copyright. All rights reserved.

10991085, 2019, 3, Downloaded from https://onlinelibrary.wiley.com/doi/10.1002/hyp.13327, Wiley Online Library on [23/01/2023]. See the Terms and Conditions (https://onlinelibrary.wiley.com/terms-and-conditions) on Wiley Online Library for rules of use; OA articles are governed by the applicable Creative Commons License

product. Both models are exceptionally flashy in the summer months. Mountain regions are characterized by variable precipitation volumes over short distances and are difficult to instrument with accurate precipitation gauges (Barry, 1994; Beniston *et al.*, 1997). In modeling complex terrain, the resolution of input precipitation datasets is a limitation that often simulates storms occurring throughout the domain simultaneously with little spatial and temporal heterogeneity. This in turn causes summer simulated flow to be more flashy than observed values. The 1km model reproduces observed peak flow volume during snowmelt, though the 100m is a better match for the only reliable baseflow curve in the Copper Creek basin (Figure 4B). Other factors specific to the land surface model may contribute to differences between observed and simulated flow. For example, Figure 2 shows that simulated snowmelt rates are slightly higher than observed.

In addition to the large East River catchment we see good model results for the smaller Copper and Rustlers catchments, particularly with respect to snowmelt timing, at the lower resolution. However, the low resolution breaks down as catchments approach the scale of the model resolution (Figure 4D). The 100m model does better at representing the smallest catchment, $1km^2$.

The sensitivity experiment was performed separately in each layer to better understand the role of geologic heterogeneity and depth in controlling flow (Table 1). Figure 5 shows the control each model layer has on flow output. On the left is a conceptual cross-section of one hillslope within the model. In Figure 5 the vertical has been exaggerated compared to the horizontal resolution in order to resolve the depth profile. The soil layer is heterogeneous with variability in *K* shown in the second column of Figure 5. The third column of Figure 5 shows weekly-averaged discharge from the 1km domain for the baseline case in black for all three layers (note, the baseline case is the same for all layers, so this line is equivalent in each plot). The shaded region represents the minimum and maximum flow in each week across all 4 hydraulic conductivity sensitivity experiments (varying initial *K* values from 0.01**K* up to 10**K*) to show the relative impact of changing hydraulic conductivity within each layer.

The soil layer has little control on flow, regardless of the *K* values selected (Figure 5). This small control in the soil layer is likely due to the small thickness (1m) relative to the geology and basement layers which affects the root distribution and therefore the evapotranspiration. The geology layer has the largest control on discharge as *K* is varied. With a very high value of *K*, flow approaches the pattern shown in Figure 4 for the 100m case, indicating baseline *K* parameters for the 100m case are much too high to match the observed peak. High *K* in the basement increases baseflow but lowering *K* beyond the baseline values does not impact baseflow significantly. This result is consistent with results from the 2D talus hillslope experiment performed in Kurylyk and Hayashi 2017. The geology layer has the opposite impact,

This article is protected by copyright. All rights reserved.

Author Manuscript

10991085, 2019, 3, Downloaded from https://onlinelibrary.wiley.com/doi/10.1002/hyp.13327, Wiley Online Library on [23/01/2023]. See the Terms and Conditions (https://onlinelibrary.wiley.com/terms-and-conditions) on Wiley Online Library for rules of use; OA articles are governed by the applicable Creative Commons License

with a lower *K* reducing baseflow volumes significantly. While the basement affects the peak flow, it controls approximately half the range that the geology layer controls.

Parameters in the geology layer are likely to have the largest impact on discharge because the geology layer interfaces with the surface, vadose zone and subsurface through transpiration of deeply rooted plants, vertical infiltration, and lateral groundwater flow. The heterogeneity in the geology layer may also produce preferential flow paths that are especially sensitive to large shifts in the magnitude of hydraulic conductivity. The geology layer is much larger than the near-surface soil layers and the basement is mostly disconnected from surface processes due to the depth of the geology layer. A different discretization of subsurface layers would likely alter layer behavior, though we chose the standard Noah LSM discretization in part so that these results could be compared to other studies. In the following discussions of specific scenario impacts we present results from the geology layer.

Figure 6 shows weekly averaged flow, change in storage, and total storage for the East River subcatchment shown in black in Figure 1. Results are shown for the geology layer of the 1km model across all four *K* scenarios. The water year has been divided into 3 seasons representing the type of flow curve produced. October to April are designated as the "baseflow" period, representing a time when flow is dominated by subsurface contributions to the stream. During the baseflow period, most temperatures are below freezing, so precipitation falls as snow and does not runoff directly. April through July are designated as the "peak flow" period, corresponding to the large increase in flow as the onset of warmer temperatures melts the snowpack built up through the winter. July to October are designated as the "summer flow" period, when discharge primarily occurs as infiltration excess in response to summer storms.

While the details and exact pattern of flow are affected by the highly heterogeneous nature of the domain and meteorological forcing dataset, it is clear that the parameterization of *K* has a patterned impact on simulated discharge (Figure 6A) and total storage (Figure 6C), and that both are driven by the seasonal changes in subsurface storage (Figure 6B). It is important to note that each of these simulations was run to a dynamic equilibrium, so each simulation is not responding to the change in *K* over the course of a single year, but has already reached a consistent annual storage amplitude; storage for each case begins and ends at the same equilibrium value (Figure 6C). While the seasonal changes in the storage curves seem small, these changes are occurring in very large reservoirs of water, on the order of 4E8 m^3. Thus, as a percentage of discharge these intra-annual changes are high in magnitude and result in hydrographs that are seasonally sensitive to *K* variability. The amount of water the subsurface maintains in dynamic equilibrium is similar for all low *K* cases, indicating that there is a lower limit to changes in subsurface storage as *K* becomes small. The 10*K* case, however, shows that total equilibrium storage is sensitive as *K* increases. There is a dramatic reduction in equilibrium storage in the 10*K* case as well as much larger seasonal storage changes shown by larger swings in the storage volumes.

This article is protected by copyright. All rights reserved.

Author Manuscript

10991085, 2019, 3, Downloaded from https://onlinelibrary.wiley.com/doi/10.1002/hyp.13327, Wiley Online Library on [23/01/2023]. See the Terms and Conditions (https://onlinelibrary.wiley.com/terms-and-conditions) on Wiley Online Library for rules of use; OA articles are governed by the applicable Creative Commons License

Author Manuscript

This effect is driven by higher *K* values, which allow more water to move into and out of storage over shorter time periods.

Higher *K* values increase the amount of discharge during the baseflow period and decrease discharge during the peak flow period, essentially flattening the hydrograph (Figure 6A). The inverse pattern can be seen in the changes in storage (Figure 6B). As K increases the subsurface absorbs the dynamic seasonal changes and reduces the surface discharge seasonality. In the 10*K* case baseflow is maintained at a higher volume, while a much larger percentage of the snowmelt pulse recharges the subsurface instead of partitioning into overland flow. The 0.01*K* case is similar to the 0.1*K* case. This result is likely due to reaching a limit- as resistance to flow in the subsurface increases, the subsurface flow moves so slowly that it does not alter streamflow at sub-annual time scales. The summer flow period does not show as strong a relationship with changing *K* as the other seasons. High *K* values do slightly reduce the flow variability and increase the storage variability in response to summer storms. The time scale of each summer monsoon rain event is much shorter, reducing the effect of subsurface parameters on surface flow until very high values of *K* are reached and interflow becomes a larger component of streamflow during short storm events.

Figure 7 shows weekly averaged flow (left column) and changes in storage (right column) for all the sub-basins shown in Figure 1. Note that the scales are different between each plot, gradually decreasing in overall flow as basin area decreases. Larger basins suggest that *K* is positively and negatively correlated with storage and discharge, respectively, as discussed in the previous paragraph and shown in Figure 6. Headwater catchments show that this relationship is weakened and complicated with decreasing drainage area. Copper, the largest sub-basin, shows a similar pattern as the full East River, where shifts in streamflow from altered *K* are mostly driven by changes in storage. However, in the 1km^2 Gothic basin the change in storage pattern is different from the flow pattern, indicating that change in storage is not the major driver of reduced streamflow. Two possible mechanisms for this difference in K control on streamflow at varying subcatchment scales are, (1) as the size of the basin decreases, the contributions to and from neighboring groundwater basins become much more significant relative to total flow, and (2) ET may play a larger role in the water balance for these very small basins. In the 10*K* case, streamflow is almost nonexistent in the smaller Rustlers and Gothic basins because the subsurface absorbs nearly the entire year's precipitation. This effect is most pronounced in Rustlers basin, a small basin with laterally-bedded sedimentary units that create preferential flow paths.

Figure 8 extends this discharge analysis by showing precipitation partitioning between evapotranspiration (ET), streamflow, and changes to subsurface storage for both the 1km and 100m models as a percentage change from the baseline case. Each season designated in Figure 6 is shown as a row in Figure 8. In the 1km model (left side of figure) we see the same impacts to

This article is protected by copyright. All rights reserved.

10991085, 2019, 3, Downloaded from https://onlinelibrary.wiley.com/doi/10.1002/hyp.13327, Wiley Online Library on [23/01/2023]. See the Terms and Conditions (https://onlinelibrary.wiley.com/terms-and-conditions) on Wiley Online Library for rules of use; OA articles are governed by the applicable Creative Commons License

discharge discussed above for Figure 6. As *K* increases, discharge during the baseflow period also increases. During the peak flow period, discharge decreases with increasing *K*, and during summer flow, discharge increases with increasing *K*.

Evapotranspiration (ET) decreases with increasing *K* in all seasons. We hypothesize that this is because as *K* increases, water can move more quickly into the subsurface, reducing plant and near-surface available moisture. However, there appears to be a limit to which *K* and ET are inversely related; below the 0.1*K* value, water continues to be available for evaporation and transpiration and the system is energy-limited. At this limit, reducing permeability no longer increases ET.

In Figure 8, the same storage pattern seen in Figure 6 is apparent. At higher *K* there is lower storage. Like the storage shown in Figure 6C, the 10*K* case has a strong effect, indicating a region of sensitivity between the baseline case (1*K*) and the 10*K* case. As *K* decreases storage does not change as quickly. This demonstrates a limit to increasing storage on sub-annual time scales; Lower *K* values slow flow into and out of the subsurface, reducing the capacity for the larger changes seen in the 10*K* case.

Moving from coarse resolution (left column in Figure 8) to the high resolution (right column in Figure 8) the same patterns persist. However, flow is less sensitive to changes in the 100m model while ET and storage are both more sensitive to changes in *K*. At finer resolution the model simulates drier soil moisture conditions, leading to a larger sensitivity in ET as soil moisture changes. This effect is partly driven by the spatial distribution of vegetation at different resolutions. In the 100m model, vegetation distribution is related to topography and water availability (Figure 3). At the 1km scale this relationship breaks down. The finely discretized grid better simulates water moving from vegetation with lower demand for water (outcropped rock, shrubs, and grasslands on hillslopes) to convergent zones in valley riparian areas that (1) demand more water and (2) have deeper rooting depths to access deeper water. This redistribution of water, driven by finer topographic and lateral resolution, to areas of higher demand, makes ET in the 100m model more sensitive to changes in *K* than ET in the 1km model, consistent with another lateral resolution study focused on evapotranspiration (Shrestha *et al.*, 2015).

At higher resolution, storage also shows much more sensitivity to changes in *K*. Microtopography is more finely resolved in the 100m model, which increases the slope for each cell. Flow is driven downhill by gravity and resisted by friction (1/*K*). Thus, subsurface flow in the higher resolution model responds not only to changes in *K*, but also to the slope term and its effect on conductivity. A conceptual model for this sensitivity mechanism is shown in Figure 10 and discussed extensively in Section 3.3. In the 100m model, the lower discharge sensitivity per increment change in *K* is driven by the higher sensitivity in storage and ET. As these water

This article is protected by copyright. All rights reserved.

Author Manuscript

10991085, 2019, 3, Downloaded from https://onlinelibrary.wiley.com/doi/10.1002/hyp.13327, Wiley Online Library on [23/01/2023]. See the Terms and Conditions (https://onlinelibrary.wiley.com/terms-and-conditions) on Wiley Online Library for rules of use; OA articles are governed by the applicable Creative Commons License

balance components become more sensitive in the heterogeneous, high-resolution domain, the sensitivity of discharge is reduced.

3.2 Manning's *n* Sensitivity

In order to identify Manning's *n* ranges that result in appropriate simulated behavior, modeled data are compared to an hourly dataset from 2016 in the same location as the Copper Creek transducer. Copper Creek is the only location that we have daily data from both water year 2006 and hourly data from 2016. Here we use the 2016 data as an analog for hourly behavior. For these comparisons, the timing of peak flow in the 2016 dataset has been shifted to match the 2006 peak.

The baseflow season does not respond significantly to changes in Manning's *n* parameters. Manning's *n* is a surface friction estimate, and has little effect on subsurface flow paths that represent the majority of discharge in the baseflow period. The Peak Flow and Summer Flow periods are more sensitive to changes in *n* (Figure 9A). Figure 9B shows behavior during the diurnal swings that characterize the snowmelt period and Figure 9C shows a storm recession during a flashy summer monsoon event.

The observed signal is very dynamic, with diurnal swings up to 22,000 m^3hr^{-1} in the peak flow period (Figure 9A). However, the oscillations in the baseline case are at least twice as large as the observed dataset throughout the year, indicating that Manning's *n* is likely underestimated in the baseline case. We hypothesize that a measured friction parameter that applies at a channel scale (1-10m) is not realistic of the total friction encountered by a stream at a 1km scale. Over 1km, a real stream would encounter channel bends and heterogeneity that could increase friction beyond the maximum for an observed channel.

While we did compare *n* from the low-end of empirically measured values (0.02) to the high end (0.2), and additionally up to 10**n* and 100**n* those values (Table 1), the more interesting comparison was the spatial distribution of *n* across the domain. The *n*-sensitivity simulations that most closely match observed streamflow diurnal oscillation volumes are those that use 10**n* (cases cn2, s10n, and ss10n from Table 1). There are large differences in response to dynamic events from peak flow diurnal swings, Figure 8B, and from summer storms, Figure 8C. The spatial distribution of *n* determines how much water reaches stream segments and how quickly overland flow generation occurs.

During peak flow, setting a spatially constant *n*=2 flattens the curve and almost eliminates the diurnal signal. Scaling *n* by vegetation everywhere results in more realistic behavior by increasing the variability of friction across the domain. This also lowers the average *n* to between

This article is protected by copyright. All rights reserved.

Author Manuscript

10991085, 2019, 3, Downloaded from https://onlinelibrary.wiley.com/doi/10.1002/hyp.13327, Wiley Online Library on [23/01/2023]. See the Terms and Conditions (https://onlinelibrary.wiley.com/terms-and-conditions) on Wiley Online Library for rules of use; OA articles are governed by the applicable Creative Commons License

Author Manuscript

0.2 and 2, decreasing total friction and allowing a more realistic response to the diurnal signal. However, this scaled case widens the width and flattens the height of the diurnal swings compared to observations. The last case, where stream segments (as defined by positive pressure in the surface cell during early summer flow) are set to a 'stream' value for Manning's n, instead of being defined by their dominant vegetation, narrows the diurnal signal to match behavior closely in the peak flow period.

Figure 9C shows a storm recession curve for a large summer storm, with observations from WY2016. As discussed in section 2.2.1, this flashy behavior is partially driven by resolution limitations in the meteorological forcing dataset, which has little variability across the domain. It is probably also driven by a faster simulated snowmelt (Figure 2). In Figure 9C the constant *n* case completely loses the recession curve on an hourly scale. The case that is scaled by vegetation gets the onset of the storm, but the peak flow is not captured and the recession is too flat. The only case that gets close to the sharp peak of the observed dataset is the scaled vegetation case with stream segments defined separately.

We do not present results from the 100m Manning's sensitivity runs here because, as shown in Figure 4, the major shape of the flow curve, especially a realistic peak flow period, needs to be reproduced before Manning's *n* hourly behavior can be assessed. It was impossible to estimate the magnitude of *n* parameters without first representing hydraulic conductivity correctly. In the next section Manning's results for both resolution models will be presented.

3.3.1. Effective Hydraulic Conductivity at Different Resolutions

The differences in streamflow between the 0.01*K* and 10*K* case shown in Figure 6A for the 1km model are similar to the differences between the 1km and 100m baseline cases shown in Figure 4. In Figure 4, as resolution increases baseflow increases and peak flow decreases. In Figure 6A, as *K* increases baseflow increases and peak flow decreases as well. The similarity in these two figures suggests that there is a relationship between *K* and lateral modeling resolution that could be used to scale model results between resolutions of the same systems.

Figure 10 shows a conceptual model of an idealized, 3km-base mountain (black triangle), discretized into three, 1km rectangles. Slopes in the discretized model are approximated by the cell center elevation, essentially reducing the slopes of the mountain block. As resolution increases, the 'Slope Estimated' shown in Figure 10 will approach the 'Slope Actual'. Therefore, a coarse resolution model will underestimate flow by underestimating the head term in Equation 1. Increasing *K* can compensate for this reduction in the gravity term by increasing the rate at which flow moves through the subsurface.

This article is protected by copyright. All rights reserved.

10991085, 2019, 3, Downloaded from https://onlinelibrary.wiley.com/doi/10.1002/hyp.13327, Wiley Online Library on [23/01/2023]. See the Terms and Conditions (https://onlinelibrary.wiley.com/terms-and-conditions) on Wiley Online Library for rules of use; OA articles are governed by the applicable Creative Commons License

Author Manuscript

Measured values for *K* vary over many orders of magnitude, making this term the most uncertain in the Darcy equation. Additionally, the concept of effective *K* to determine variation in *K* at different scales is already in use. For these reasons, it makes sense to include the loss of topographic information from coarsening resolution in the *K* term of the Darcy flux. Here we present an effective *K* term, shown by Equation 6, that incorporates the slope aspect in each cell. The $sin\theta$ term in Equation 3 is the vertical component of the slope, representing the contribution of gravity to flow.

EQUATION 6:

$$K_{eff} = sin\theta K$$

θ: Local angle of slope (-)
K_{eff}: Effective hydraulic conductivity
K: Actual hydraulic conductivity

K_{eff} is not equivalent to *K*, but rather a term that biases the flow upwards to compensate for the loss in gravity term as slopes are flattened in a topographically complex setting. As resolution increases and approaches the actual slope (Figure 10), K_{eff} will approach *K* and slope adjustments will approach one, leaving the original Darcy equation (Equation 1). This method thus allows for a scaling of process changes across resolution without disturbing the underlying mathematics.

The sensitivity results presented in section 3.1 and 3.2 show that the parameters for the baseline run cases, chosen based on the only large-scale dataset available, were relatively successful at modeling flow at 1km resolution. This is not an indication, however, that the *K* values match the real *K* values in the field, but rather that they are good choices for K_{eff} that would be required to compensate for the loss of slope aspect in the 1km model. Results at 100m indicated that more resistance to flow was needed to match observed behavior. Figure 11 presents a breakdown of how this might occur based on the conceptual model presented in Figure 10. Figure 11A and B are similar to the 1km and 100m geology layer plots shown in Figure 2, except instead of plotting geologic units, *K* values are plotted in Figure 11. The difference between 1km and 100m hydraulic conductivities is plotted in Figure 11C, with a mean value of 0.0057. Figure 11D and E show K_{eff} values, incorporating the contribution of slope into the *K* term. The difference plot of K_{eff} (Figure 11F) is much larger than the difference plot of *K* (Figure 11C), with a mean value of 0.013 instead of 0.0057. Though Figure 11F is plotted at 100m resolution, the coarse resolution grid is discernable because the topography was simplified most at the edges of the coarse grid, resulting in large differences in K_{eff}.

In order to determine the best K_{eff} value to match simulated and observed flow behavior in the 100m model, we determine a scalar that minimizes the ratio between 100m K_{eff} and 1km K_{eff}. If the slopes matched exactly between the 1km and 100m models, then the ratio between the two

This article is protected by copyright. All rights reserved.

10991085, 2019, 3, Downloaded from https://onlinelibrary.wiley.com/doi/10.1002/hyp.13327, Wiley Online Library on [23/01/2023]. See the Terms and Conditions (https://onlinelibrary.wiley.com/terms-and-conditions) on Wiley Online Library for rules of use; OA articles are governed by the applicable Creative Commons License

would be 1, so for each geologic layer the expression shown in Equation 7 was minimized to determine a single scaling factor from K to K_{eff}.

EQUATION 7:

$$minimum = s\ (\mathbf{1} - \frac{K_{eff}100m}{K_{eff}1km})$$

s: scalar value used to minimize the expression shown in the right half of Equation 7.

The effect of minimizing error using Equation 7 is shown in Figure 12 and the resulting improvement in flow representation is shown in Figure 13. Figure 12A shows the error in the heterogeneous geology layer between the 1km and 100m K_{eff} ratios using the original parameter set for K. Figure 12B shows the resulting reduction in error after scaling K by the value determined in Equation 7. This methodology was used to scale the basement and geology layers of the model. Soil parameters were not scaled because the impact on flow from changes to soil conductivities is small and mostly based on a threshold for resisting flow to the subsurface, not on subsurface transport within the thin soil layer (Figure 5). Ultimately the scaling factor determined by Equation 7 was 0.070 for the basement layer and 0.061 for the geology layer. The resulting improvement in matching flow between the 1km and 100m models is shown in Figure 13.

A similar relationship between subsurface flow parameters and resolution was developed by Niedda, 2004 for a simplified subsurface (soil K decreases with depth) and routed overland flow. The author quantifies the information loss as spatial scale is aggregated using the entropy of terrain curvature, then relates this measure to their parameter for decay of hydraulic conductivity with depth. This work extends this concept to integrated modeling of streamflow in a real basin where K distributions are defined by geology.

Many factors play a role in determining streamflow volumes at different resolutions. These include all parameters involved, including geology aggregation (K), the stream network that is generated by slope processing at different resolutions, the sub-basin watershed discretization, landcover aggregation, and meteorological forcing inputs. In order to determine how generalizable the method was at different resolutions we constructed two additional models of the domain at 250m and 500m resolution. As expected, the slopes increase in every effective K case shown in Table 2, though resulting streamflow representation does not reach 1:1 in every case. This demonstrates that the method consistently biases streamflow to be more dynamic, but that other factors play a larger role as the difference between resolutions becomes smaller. The success of the 1km to 100m scaling suggests that for large changes in resolution, topographic gradients dominate the streamflow changes between resolutions. As the change in resolution is reduced, the ability of a single parameter adjustment to compensate for differences in flow is reduced. Figure 14 shows the density plots of slope at each modeling resolution. The coarse

This article is protected by copyright. All rights reserved.

Author Manuscript

10991085, 2019, 3, Downloaded from https://onlinelibrary.wiley.com/doi/10.1002/hyp.13327, Wiley Online Library on [23/01/2023]. See the Terms and Conditions (https://onlinelibrary.wiley.com/terms-and-conditions) on Wiley Online Library for rules of use; OA articles are governed by the applicable Creative Commons License

resolution model peaks at the flatter end of the slope axis, while the other three resolution models spread more consistently across the entire range. The large difference between slopes in the 100m and 1km models could be used as an indicator that this first-order correction using K_{eff} will be useful at these specific resolutions. This also suggests that the method may not be applicable in a different topographic setting where slope density changes with resolution are smaller. In the great plains of the United States, for example, slope aspect has a relatively small impact on flow compared to landcover and geologic heterogeneity. This scaling method is likely most useful in regions of topographic complexity where slope is a large contributor to streamflow.

3.3.2. Determining Manning's *n* Parameters at Different Resolutions

Nineteen additional modeling runs were conducted in both the 1km and 100m domains that combined new hydraulic conductivity parameters with different methods of scaling of Manning's *n* values between resolutions. Despite these tests, no reliable mathematical method was found to scale Manning's *n* between lateral resolution.

The Manning's equation (Equation 4) mostly impacts streamflow on timescales of seconds to days (Figure 9). This experiment updates pressure calculations at hourly timesteps for an entire year. It is therefore possible that no Manning's *n* relationship could be determined because the *n* parameter could be more or equally sensitive to time discretization than to lateral spatial resolution. Further study varying time discretization and *n* would be useful to determine if an effective Manning's *n* parameter could be determined based on both the time and spatial discretization chosen. We hope that new studies in real domains will explore both time and space discretization. Continued research in this area may help determine a systematic relationship that could be used to scale this important parameter.

Based on the resulting flow output from the Manning's *n* simulations after the 100m hydraulic conductivity was determined, Manning's *n* values were chosen that most closely balanced matching hourly flow recessions (as in Figure 9) with minimizing flashy behavior. As discussed in Section 3.2, the simulation most closely mimicked observed hourly streamflow when *n* reflected both vegetation distribution and stream cells. This distribution was used in the final parameter set for both the 1km and 100m model. As discussed in Section 3.2, the 10**n* magnitude best matched flow at 1km resolution. In the 100m model, a scaling factor of 50**n* was used. The resulting flow from these final parameters are also shown in Figure 12 for each basin. In the absence of a scaling mechanism, sensitivity studies like this can help inform parameter choices in models where empirical values may not apply.

4. Conclusions

This article is protected by copyright. All rights reserved.

Author Manuscript

10991085, 2019, 3, Downloaded from https://onlinelibrary.wiley.com/doi/10.1002/hyp.13327, Wiley Online Library on [23/01/2023]. See the Terms and Conditions (https://onlinelibrary.wiley.com/terms-and-conditions) on Wiley Online Library for rules of use; OA articles are governed by the applicable Creative Commons License

The sensitivity results presented here compared Manning's *n* and hydraulic conductivity parameters (*K*) over 4 orders of magnitude in a real, 255km^2 mountain domain at both 1km and 100m resolution. These results suggest that as resolution is coarsened, *K* needs to be biased higher in order to continue to represent the dynamic streamflow response in a topographically complex domain. We present a mathematical methodology for scaling hydraulic conductivity (*K*) across different modeling resolutions in order to create this bias. The method uses an effective *K* value to simultaneously address uncertainty in *K* and loss of topographic gradients in coarsening resolution. These sensitivity results document the changes to process representation across scale in physically-based models of complex mountain regions, reinforcing two prior findings and documenting 3 new findings, specifically:

- Figure 6 shows that as *K* increases in magnitude baseflow increases and peak flow during snowmelt decreases. We observed the opposite behavior as *K* decreases. These results suggest that *K* acts as a moderator between rapid subsurface response (high *K*) and rapid streamflow response (low *K*), extending hillslope-scale results showing similar controls on a diurnal timescale (Kurylyk and Hayashi, 2017).
- Figure 5 demonstrates that streamflow sensitivity to *K* depends most on the subsurface units, with the 8m geology layer showing the largest sensitivity to changes. The basement layer exhibits approximately 50% of the sensitivity in the geology layer to the same changes in *K*. The soil layer shows little sensitivity to change and this may be due to the small width of the soil layer (1m) compared to the geology (8m) or the basement (21m).
- Manning's *n* influences discharge over shorter timescales than *K*. Runoff was sensitive to both magnitude and spatial distribution of *n*. A heterogeneous *n* defined by vegetation was critical to matching behavior, as well as defining a separate value for *n* within the stream network. While the magnitude of *n* did depend on the grid resolution, a distinct scaling relationship did not emerge from this experiment.
- As resolution is coarsened, topography is averaged, reducing the slope term in the Darcy flux (Figure 10). Figures 11 and 12 show that incorporating changes to the topographic gradients as scale changes into an effective *K* parameter allows for improved flow representation at different modeling grid resolutions. The concept of effective *K* is well documented in the literature and makes a better parameter than measured *K* for physically based models. This scaling procedure is robust in that, as resolution increases, the Darcy equation approaches measured processes known to be accurate on 1-10m scales, without requiring any change to the underlying physics of the model. This shows both a scale-dependence of effective *K* and also a useful approach for transferability of parameters across resolution. For example, a parameter estimation conducted at coarse resolution with a less computationally expensive model may then be scaled to the higher resolution simulation.

This article is protected by copyright. All rights reserved.

Author Manuscript

10991085, 2019, 3, Downloaded from https://onlinelibrary.wiley.com/doi/10.1002/hyp.13327, Wiley Online Library on [23/01/2023]. See the Terms and Conditions (https://onlinelibrary.wiley.com/terms-and-conditions) on Wiley Online Library for rules of use; OA articles are governed by the applicable Creative Commons License

Author Manuscript

Models do inherently simplify processes, and often changing resolutions, whether by approaching hyper-resolution models or by scaling coarse resolutions to larger areas, can alter the way processes are represented. The results presented here are most effective in topographically complex regions and when making large changes in lateral resolutions. There are numerous parameters that affect modeled flow output that were not discussed here and these may have a larger influence in other regions where topography is not the main driver of response. While *K* and *n* are sensitive, each parameter involved is likely to be sensitive in a particular situation, necessitating continuous integration of measured field parameters, modeled output, and comparison to observations to best understand these complex systems.

Modeling provides a unique environment where the mathematical scaling of physical processes can be explicitly explored at all simulated times and simulated spatial extents, an opportunity that is not available in field observations. If these scaling patterns are explored further, model parameterization can be continuously improved. This is especially important to the development of computationally expensive physically-based models, where traditional calibration techniques are impossible to apply. As hydrologists work towards the modeling Grand Challenge described by Wood *et al* 2011a, there is an increasing need for new methodologies for parameter selection. Understanding the scaling of processes like runoff generation in response to shifts in parameters helps to address some of the uncertainties and challenges posed by computationally demanding modeling efforts.

5. Acknowledgements

This study was funded by a National Science Foundation Blue Waters Fellowship under award numbers ACI-0725070 and ACI-1238993, Department of Energy Office of Science Graduate Student Research Award under award DE-SC0014664), and as part of the Watershed Function Scientific Focus Area funded by the U.S. Department of Energy, Office of Science, Office of Biological and Environmental Research under Award Number DE-AC02-05CH11231.

6. References

Ala-aho P, Soulsby C, Wang H, Tetzlaff D. 2017. Integrated surface-subsurface model to investigate the role of groundwater in headwater catchment runoff generation: A minimalist approach to parameterisation. *Journal of Hydrology* **547**: 664–677 DOI: 10.1016/j.jhydrol.2017.02.023

Barnett TP, Adam JC, Lettenmaier DP. 2005. Potential impacts of a warming climate on water availability in snow-dominated regions. *Nature* **438** (7066): 303–309 DOI: 10.1038/nature04141

This article is protected by copyright. All rights reserved.

10991085, 2019, 3, Downloaded from https://onlinelibrary.wiley.com/doi/10.1002/hyp.13327, Wiley Online Library on [23/01/2023]. See the Terms and Conditions (https://onlinelibrary.wiley.com/terms-and-conditions) on Wiley Online Library for rules of use; OA articles are governed by the applicable Creative Commons License

Author Manuscript

Barry RG. 1994. Past and potential future changes in mountain environments: a review. In *Beniston, M., Ed. Routledge Publishing Company, London and New York*3–33.

Battaglin W a., Hay LE, Markstrom SL. 2012. Watershed Scale Response to Climate Chage - East River Basin, Colorado. *USGS Publication* (March)

Beniston M. 2003. Climatic Change in Mountain Regions *Climate Change* **59**: 5–31

Beniston M, Diaz HF, Bradley RS. 1997. Climatic Change At High Elevation Sites: an Overview. *Climatic Change* **36** (3): 233–251 DOI: 10.1023/A:1005380714349

Beven KJ, Cloke HL. 2012. Comment on 'hyperresolution global land surface modeling: Meeting a grand challenge for monitoring Earth's terrestrial water' by Eric F. Wood et al. *Water Resources Research* **48** (1): 2–4 DOI: 10.1029/2010WR010090

Bierkens MFP, Bell VA, Burek P, Chaney N, Condon LE, David CH, Roo A, D"oll P, Drost N, Famiglietti JS, et al. 2015. Hyper -resolution glob *Hydrological Processes* **29** (2): 310–320 DOI: 10.1002/hyp.10391

Bormann H. 2006. Impact of spatial data resolution on simulated catchment water balances and model performance of the multi-scale TOPLATS model. *Hydrology and Earth System Sciences* **10** (2): 165–179 DOI: 10.5194/hess-10-165-2006

Brace WF. 1980. Permeability of crystalline and argillaceous rocks. *International Journal of Rock Mechanics and Mining Sciences & Geomechanics Abstracts* **17** (5): 241–251 DOI: 10.1016/0148-9062(80)90807-4

Brutsaert W. 2008. *Hydrology: an introduction. 3rd ed*. DOI: 10.2277/0521824796

Carroll RWH, Bearup LA, Brown W, Willlams KH. 2018. Factors controlling seasonal groundwater and solute flux from snow –16 dominated basins. (Nov 10.1002/hyp.13151

Chen F, Dudhia J. 2001. Coupling an Advanced Land Surface–Hydrology Model with the Penn State–NCAR MM5 Modeling System. Part II: Preliminary Model Validation. *Monthly Weather Review* **129** (4): 587–604 DOI: 10.1175/1520-0493(2001)129<0587:CAALSH>2.0.CO;2

Clauser C. 1992. Permeability of crystalline rocks. *Eos, Transactions American Geophysical Union* **73** (21): 233–233 DOI: 10.1029/91EO00190

Cosgrove BA. 2003. Real-time and retrospective forcing in the North American Land Data Assimilation System (NLDAS) project. *Journal of Geophysical Research* **108** (D22): 8842 DOI: 10.1029/2002JD003118

Dixon B, Earls J. 2009. Resample or not?! Effects of resolution of DEMs in watershed modeling. *Hydrological Processes* (April 2009): 1714–1724 DOI: 10.1002/hyp

Domenico PA, Schwartz FW. 1997. *Physical and chemical hydrogeology. Second edition*. Available at: http://www.scopus.com/inward/record.url?eid=2-s2.0-0031884855&partnerID=tZOtx3y1

Ferguson IM, Jefferson JL, Maxwell RM, Kollet SJ. 2016. Effects of root water uptake formulation on simulated water and energy budgets at local and basin scales. *Environmental Earth Sciences* **75** (4) DOI: 10.1007/s12665-015-5041-z

This article is protected by copyright. All rights reserved.

10991085, 2019, 3, Downloaded from https://onlinelibrary.wiley.com/doi/10.1002/hyp.13315 by Wiley Online Library on [23/01/2023]. See the Terms and Conditions (https://onlinelibrary.wiley.com/terms-and-conditions) on Wiley Online Library for rules of use; OA articles are governed by the applicable Creative Commons License

Author Manuscript

Freeze, R.A., Cherry JA. 1979. *Groundwater*.

Gelhar LW, Welty C, Rehfeldt KR. 1992. A Critical Review of Data on Field-Scale Dispersin in Aquifers. *Water Resources Research* **28** (7): 1955–1974 DOI: 10.1029/92WR00607

Giertz S, Diekkrüger B, Steup G. 2006. Physically-based modelling of hydrological processes in a tropical headwater catchment in Benin (West Africa) – process representation and multi-criteria validation. *Hydrology and Earth System Sciences* **3** (2005): 595–651 DOI: 10.5194/hessd-3-595-2006

Gilbert J, Jefferson J, Constantine PG, Maxwell R. 2016. Global spatial sensitivity of runoff to subsurface permeability using the active subspace method. *Advances in Water Resources* **92**: 30–42 DOI: 10.1016/j.advwatres.2016.03.020

Gleeson T, Smith L, Moosdorf N, Hartmann J, D''urr HH, Manning AH, van Beek LPH, Jellinek AM. 2011. Mapping permeability over the surface of the Earth. *Geophysical Research Letters* DOI: 10.1029/2010GL045565

von Gunten D, Wöhling T, Haslauer C, Merchán D, Causapé J, Cirpka OA. 2014. Efficient calibration of a distributed pde-based hydrological model using grid coarsening. *Journal of Hydrology* **519** (PD): 3290–3304 DOI: 10.1016/j.jhydrol.2014.10.025

Ikeda K, Rasmussen R, Liu C, Gochis D, Yates D, Chen F, Tewari M, Barlage M, Dudhia J, Miller K, et al. 2010. Simulation of seasonal snowfall over Colorado. *Atmospheric Research* **97** (4): 462–477 DOI: 10.1016/j.atmosres.2010.04.010

Jana RB, Mohanty BP. 2012. A comparative study of multiple approaches to soil hydraulic parameter scaling applied at the hillslope scale. **48** (July 2011): 1–16 DOI: 10.1029/2010WR010185

Jefferson J, Maxwell RM. 2015. Evaluation of simple to complex parameterizations of bare ground evaporation. *Journal of Advances in Modeling Earth Systems* **7**: 513–526 DOI: 10.1002/2013MS000282.Received

Jefferson J, Gilbert J, Constantine P, Maxwell R. 2015a. Active subspaces for sensitivity analysis and dimension reduction of an integrated hydrologic model. *Computers & Geosciences* **83**: 127–138 DOI: 10.1016/j.cageo.2015.07.001

Jefferson J, Gilbert J, Constantine P, Maxwell R. 2015b. Active subspaces for sensitivity analysis and dimension reduction of an integrated hydrologic model. *Computers & Geosciences* **83**: 127–138 DOI: 10.1016/j.cageo.2015.07.001

Kollet SJ, Maxwell RM. 2006. Integrated surface–groundwater flow modeling: A free-surface overland flow boundary condition in a parallel groundwater flow model. *Advances in Water Resources* **29** (7): 945958 DOI: 10.1016/j.advwatres.2005.08.006

Kurylyk BL, Hayashi M. 2017. Inferring hydraulic propertites of alpine aquifers from the propagation of diurnal snowmelt signals: 237–256 DOI: 10.1002/2016WR019538.Received

Markovich KH, Maxwell RM, Fogg GE. 2016. Hydrogeological response to climate change in alpine hillslopes. *Hydrological Processes*: n/a-n/a DOI: 10.1002/hyp.10851

Maxwell RM. 2013. A terrain-following grid transform and preconditioner for parallel, large-scale, integrated hydrologic modeling. *Advances in Water Resources* **53**: 109117 DOI:

This article is protected by copyright. All rights reserved.

10991085, 2019, 3, Downloaded from https://onlinelibrary.wiley.com/doi/10.1002/hyp.13327, Wiley Online Library on [23/01/2023]. See the Terms and Conditions (https://onlinelibrary.wiley.com/terms-and-conditions) on Wiley Online Library for rules of use; OA articles are governed by the applicable Creative Commons License

10.1016/j.advwatres.2012.10.001
Maxwell RM, Condon LE. 2016. Connections between groundwater flow and transpiration partitioning. *Science* **353** (6297): 377–380 DOI: 10.1126/science.aaf7891
Maxwell RM, Miller NL. 2005. Development of a Coupled Land Surface and Groundwater Model. *Journal of Hydrometeorology* **6** (3): 233247 DOI: 10.1175/JHM422.1
Maxwell RM, Condon LE, Kollet SJ. 2015. A high-resolution simulation of groundwater and surface water over most of the continental US with the integrated hydrologic model ParFlow v3. *Geoscientific Model Development* **8** (3): 923–937 DOI: 10.5194/gmd-8-923-2015
McCabe GJ, Hay LE. 1995. Hydrological effects of hypothetical climate change in the East River basin, Colorado, USA. *Hydrological Sciences Journal* **40** (3): 303–318 DOI: 10.1080/02626669509491417
Mitchell KE. 2004. The multi-institution North American Land Data Assimilation System (NLDAS): Utilizing multiple GCIP products and partners in a continental distributed hydrological modeling system. *Journal of Geophysical Research* **109** (D7): D07S90 DOI: 10.1029/2003JD003823
Niedda M. 2004. Upscaling hydraulic conductivity by means of entropy of terrain curvature representation. *Water Resources Research* **40** (4): 1–16 DOI: 10.1029/2003WR002721
Pan M, Cai X, Chaney NW, Entekhabi D, Wood EF. 2016. An initial assessment of SMAP soil moisture retrievals using high-resolution model simulations and in situ observations. *Geophysical Research Letters* **43** (18): 9662–9668 DOI: 10.1002/2016GL069964
Peckarsky BL, McIntosh AR, Horn SC, McHugh K, Booker DJ, Wilcox AC, Brown W, Alvarez M. 2014. Characterizing disturbance regimes of mountain streams. *Freshwater Science* **33** (3): 716–730 DOI: 10.1086/677215
Pepin N, Bradley RS, Diaz HF, Baraer M, Caceres EB, Forsythe N, Fowler H, Greenwood G, Hashmi MZ, Liu XD, et al. 2015. Elevation-dependent warming in mountain regions of the world. *Nature Climate Change* **5** (5): 424–430 DOI: 10.1038/nclimate2563
Robinson D a, Binley A, Hubbard SS, Huisman J a. 2015. The Emergence of Hydrogeophysics for Improved Understanding of Subsurface Processes Over Multiple Scales. *Water Resources Research*: 1–30 DOI: 10.1002/2015WR017016.Received
Sciuto G, Diekkrüger B. 2010. Influence of Soil Heterogeneity and Spatial Discretization on Catchment Water Balance Modeling. *Vadose Zone Journal* **9** (4): 955 DOI: 10.2136/vzj2009.0166
Shrestha P, Sulis M, Simmer C, Kollet S. 2015. Impacts of grid resolution on surface energy fluxes simulated with an integrated surface-groundwater flow model. *Hydrology and Earth System Sciences* **19** (10): 4317–4326 DOI: 10.5194/hess-19-4317-2015
Srivastava V, Graham W, Muñoz-Carpena R, Maxwell RM. 2014. Insights on geologic and vegetative controls over hydrologic behavior of a large complex basin - Global Sensitivity Analysis of an integrated parallel hydrologic model. *Journal of Hydrology* **519** (PB): 2238–2257 DOI: 10.1016/j.jhydrol.2014.10.020

Author Manuscript

This article is protected by copyright. All rights reserved.

10991085, 2019, 3, Downloaded from https://onlinelibrary.wiley.com/doi/10.1002/hyp.13327, Wiley Online Library on [23/01/2023]. See the Terms and Conditions (https://onlinelibrary.wiley.com/terms-and-conditions) on Wiley Online Library for rules of use; OA articles are governed by the applicable Creative Commons License

Sudicky EA, Huyakorn PS. 1991. Contaminant Migration in Imperfectly Known Heterogeneous Groundwater Systems. *Reviews of Geophysics* **29** (April): 240–253

Sulis M, Paniconi C, Camporese M. 2011. Impact of grid resolution on the integrated and distributed response of a coupled surface-subsurface hydrological model for the des Anglais catchment, Quebec. *Hydrological Processes* **25** (12): 1853–1865 DOI: 10.1002/hyp.7941

Vivoni ER, Ivanov VY, Bras RL, Entekhabi D. 2005. On the effects of triangulated terrain resolution on distributed hydrologic model response. *Hydrological Processes* **19** (11): 2101–2122 DOI: 10.1002/hyp.5671

Welch LA, Allen DM. 2014. Hydraulic conductivity characteristics in mountains and implications for conceptualizing bedrock groundwater flow. *Hydrogeology Journal* **22** (5): 10031026 DOI: 10.1007/s10040-014-1121-5

Williams KH. RMM. 2017. Spoken Communication

Winnick MJ, Carroll RWH, Williams KE, Maxwell, Reed M, Dong W, Maher K. 2017. Snowmelt controls on concentration-discharge relationships and the balance of oxidative and acid-base weathering fluxes in an alpine catchment, East River, Colorado. *Water Resources Research* **53**: 2507–2523 DOI: 10.1002/2016WR019724.Received

Wood AW, Leung LR, Sridhar V, Lettenmaier DP. 2004. Hydrologic implications of dynamical and statistical approaches to downscaling climate model outputs. *Climatic Change* **62** (1–3): 189–216 DOI: 10.1023/B:CLIM.0000013685.99609.9e

Wood EF, Roundy JK, Troy TJ, van Beek LPH, Bierkens MFP, Blyth E, de Roo A, D"oll P, Ek M, Famiglietti J, et al. 2011a. Hyperresolution global land surface modeling: Meeting a grand challenge for monitoring Earth's terrestrial water. *Water Resources Research* **47** (5) DOI: 10.1029/2010WR010090

Wood EF, Roundy JK, Troy TJ, van Beek LPH, Bierkens MFP, Blyth E, de Roo A, Döll P, Ek M, Famiglietti J, et al. 2011b. Hyperresolution global land surface modeling: Meeting a grand challenge for monitoring Earth's terrestrial water. *Water Resources Research* **47** (5): W05301 DOI: 10.1029/2010WR010090

Zhang W, Montgomery DR. 1994. Digital elevation model grid size, landscape representation, and hydrologic simulations. *Water Resources Research* **30** (4): 1019–1028 DOI: 0043.1397/94/93WR-03553505.00

Zheng C, Gorelick SM. 2003. Analysis of solute transport in flow fields influenced by preferential flowpaths at the decimeter scale. *Ground Water* **41** (2): 142–155 DOI: 10.1111/j.1745-6584.2003.tb02578.x

Author Manuscript

This article is protected by copyright. All rights reserved.

10991085, 2019, 3, Downloaded from https://onlinelibrary.wiley.com/doi/10.1002/hyp.13327, Wiley Online Library on [23/01/2023]. See the Terms and Conditions (https://onlinelibrary.wiley.com/terms-and-conditions) on Wiley Online Library for rules of use; OA articles are governed by the applicable Creative Commons License

Author Manuscript

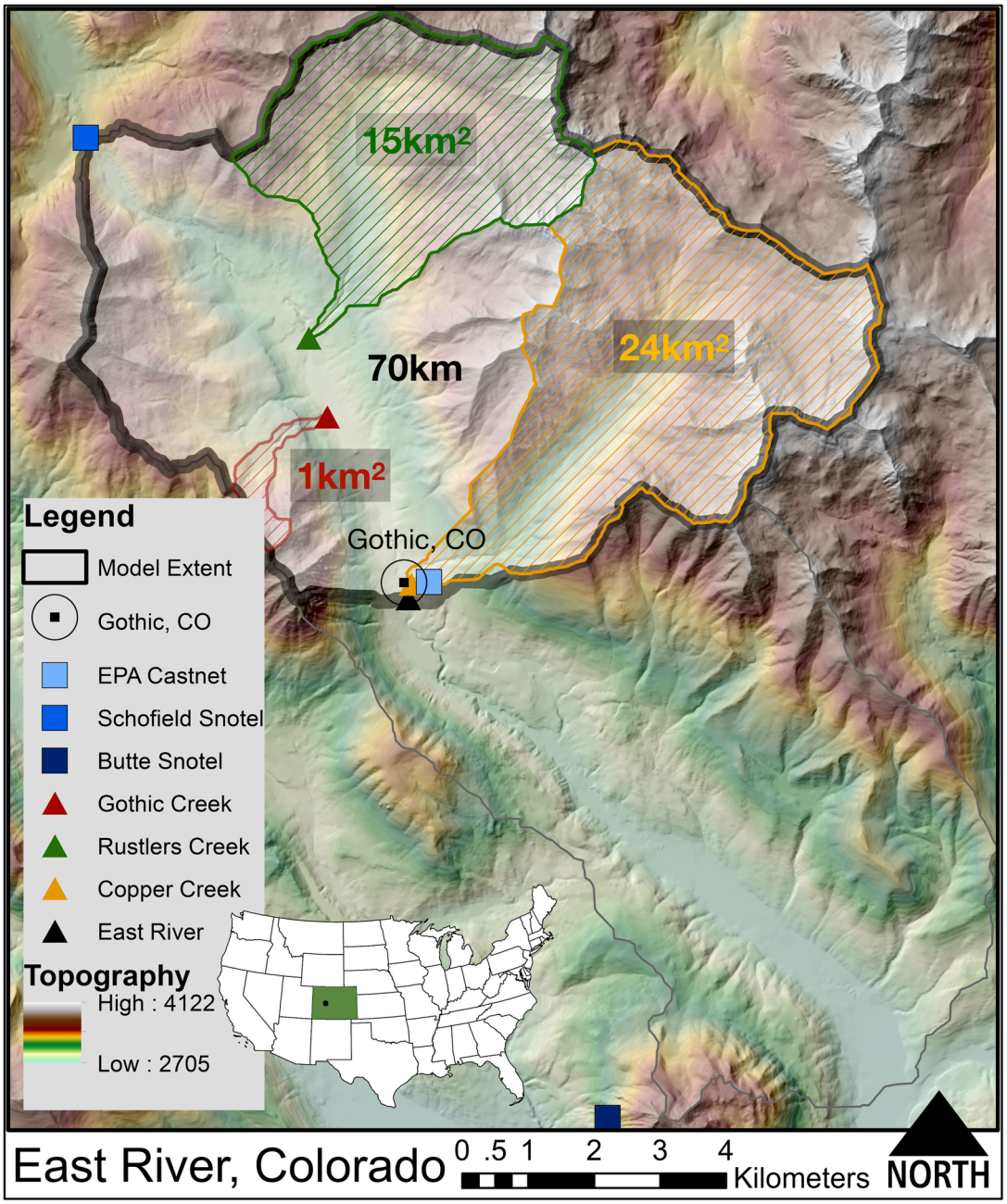

FIGURE 1: East River model area (entire figure) and catchment. Locations where observations for water year 2006 are marked including two SNOTEL stations, one EPA Castnet station, and four pressure transducers with their upstream area outlined.

HYP_13327_F1.tiff

This article is protected by copyright. All rights reserved.

10991085, 2019, 3, Downloaded from https://onlinelibrary.wiley.com/doi/10.1002/hyp.13327, Wiley Online Library on [23/01/2023]. See the Terms and Conditions (https://onlinelibrary.wiley.com/terms-and-conditions) on Wiley Online Library for rules of use; OA articles are governed by the applicable Creative Commons License

Author Manuscript

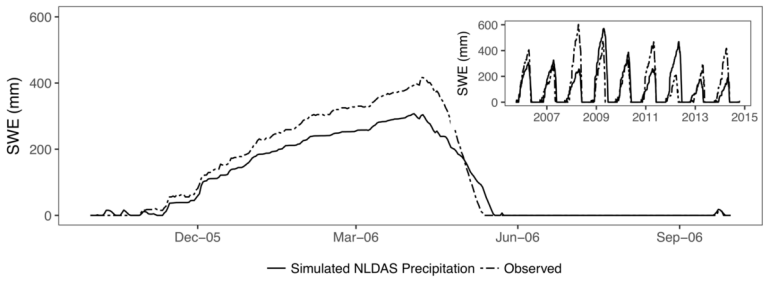

HYP_13327_F2.tiff

This article is protected by copyright. All rights reserved.

10991085, 2019, 3, Downloaded from https://onlinelibrary.wiley.com/doi/10.1002/hyp.13327, Wiley Online Library on [23/01/2023]. See the Terms and Conditions (https://onlinelibrary.wiley.com/terms-and-conditions) on Wiley Online Library for rules of use; OA articles are governed by the applicable Creative Commons License

Author Manuscript

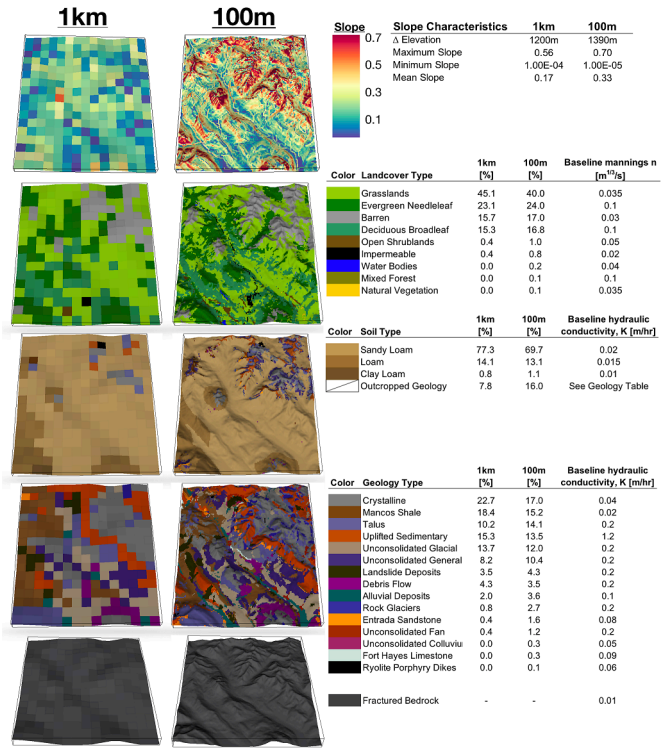

FIGURE 3: Input datasets for 1km and 100m models.

HYP_13327_F3.tif

This article is protected by copyright. All rights reserved.

10991085, 2019, 3, Downloaded from https://onlinelibrary.wiley.com/doi/10.1002/hyp.13327, Wiley Online Library on [23/01/2023]. See the Terms and Conditions (https://onlinelibrary.wiley.com/terms-and-conditions) on Wiley Online Library for rules of use; OA articles are governed by the applicable Creative Commons License

Author Manuscript

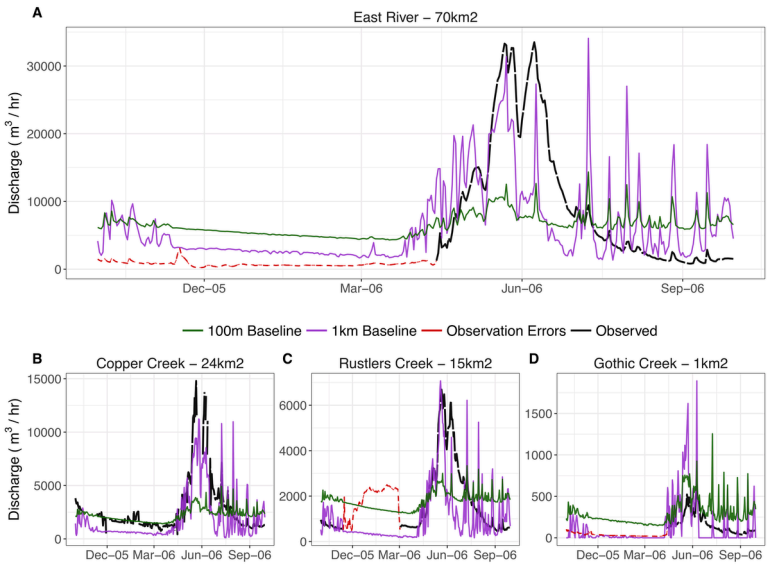

HYP_13327_F4.tiff

This article is protected by copyright. All rights reserved.

10991085, 2019, 3, Downloaded from https://onlinelibrary.wiley.com/doi/10.1002/hyp.13327, Wiley Online Library on [23/01/2023]. See the Terms and Conditions (https://onlinelibrary.wiley.com/terms-and-conditions) on Wiley Online Library for rules of use; OA articles are governed by the applicable Creative Commons License

Author Manuscript

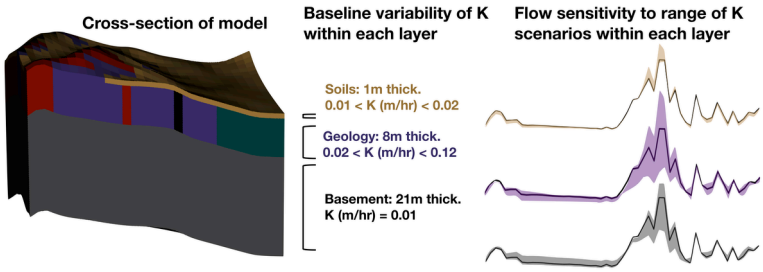

HYP_13327_F5.tiff

This article is protected by copyright. All rights reserved.

10991085, 2019, 3, Downloaded from https://onlinelibrary.wiley.com/doi/10.1002/hyp.13327, Wiley Online Library on [23/01/2023]. See the Terms and Conditions (https://onlinelibrary.wiley.com/terms-and-conditions) on Wiley Online Library for rules of use; OA articles are governed by the applicable Creative Commons License

Author Manuscript

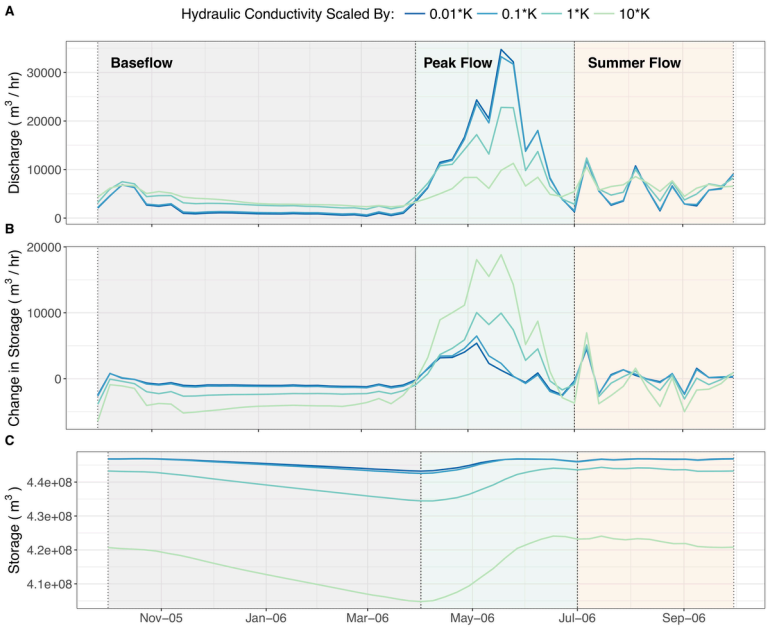

HYP_13327_F6.tiff

This article is protected by copyright. All rights reserved.

10991085, 2019, 3, Downloaded from https://onlinelibrary.wiley.com/doi/10.1002/hyp.13327, Wiley Online Library on [23/01/2023]. See the Terms and Conditions (https://onlinelibrary.wiley.com/terms-and-conditions) on Wiley Online Library for rules of use; OA articles are governed by the applicable Creative Commons License

Author Manuscript

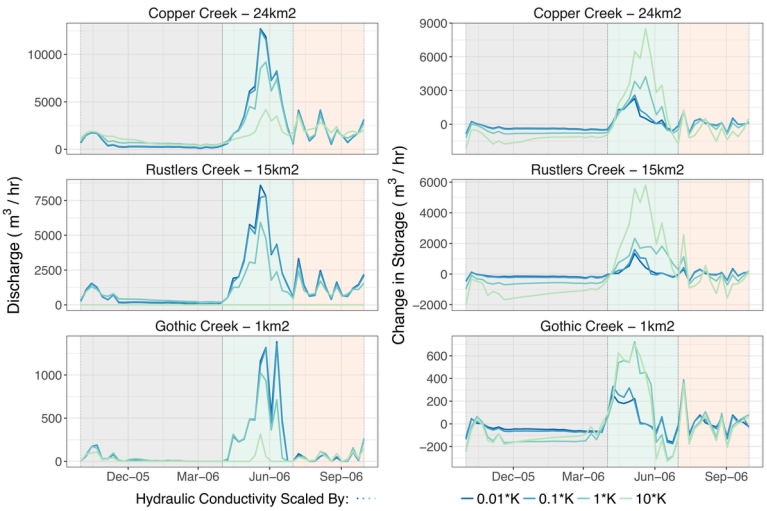

HYP_13327_F7.tiff

This article is protected by copyright. All rights reserved.

10991085, 2019, 3, Downloaded from https://onlinelibrary.wiley.com/doi/10.1002/hyp.13327, Wiley Online Library on [23/01/2023]. See the Terms and Conditions (https://onlinelibrary.wiley.com/terms-and-conditions) on Wiley Online Library for rules of use; OA articles are governed by the applicable Creative Commons License

Author Manuscript

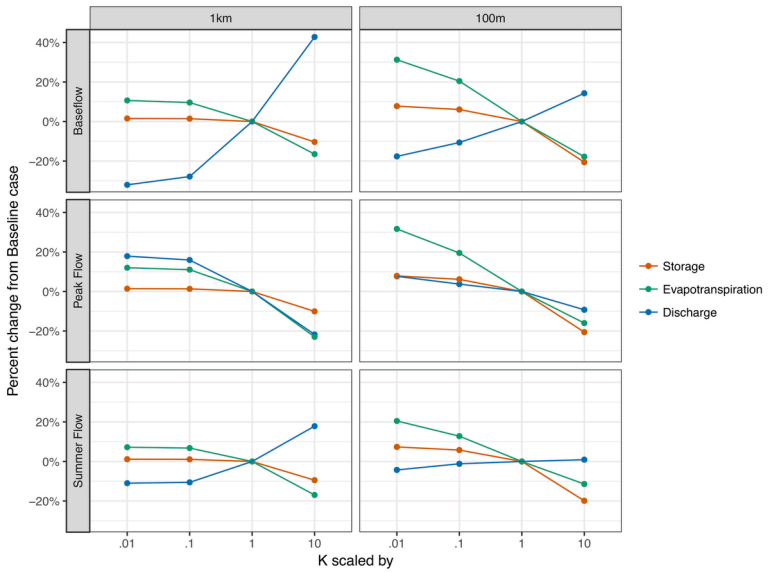

HYP_13327_F8.tiff

This article is protected by copyright. All rights reserved.

10991085, 2019, 3, Downloaded from https://onlinelibrary.wiley.com/doi/10.1002/hyp.13327, Wiley Online Library on [23/01/2023]. See the Terms and Conditions (https://onlinelibrary.wiley.com/terms-and-conditions) on Wiley Online Library for rules of use; OA articles are governed by the applicable Creative Commons License

Author Manuscript

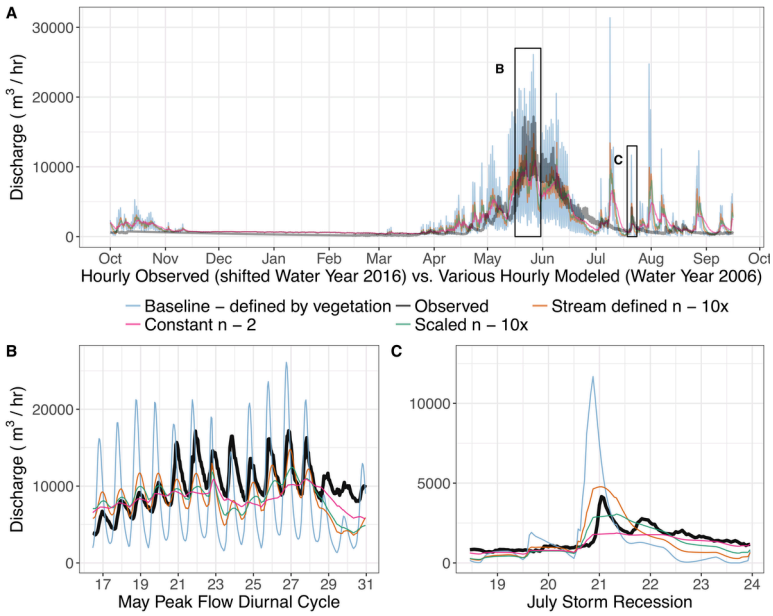

HYP_13327_F9.tiff

This article is protected by copyright. All rights reserved.

10991085, 2019, 3, Downloaded from https://onlinelibrary.wiley.com/doi/10.1002/hyp.13327, Wiley Online Library on [23/01/2023]. See the Terms and Conditions (https://onlinelibrary.wiley.com/terms-and-conditions) on Wiley Online Library for rules of use; OA articles are governed by the applicable Creative Commons License

Author Manuscript

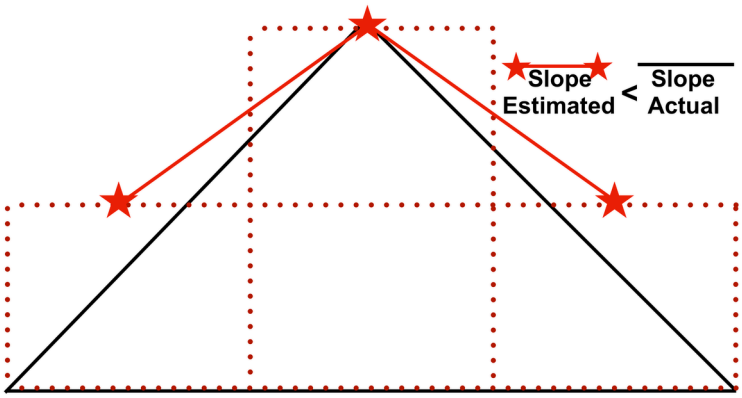

HYP_13327_F10.tiff

This article is protected by copyright. All rights reserved.

10991085, 2019, 3, Downloaded from https://onlinelibrary.wiley.com/doi/10.1002/hyp.13327, Wiley Online Library on [23/01/2023]. See the Terms and Conditions (https://onlinelibrary.wiley.com/terms-and-conditions) on Wiley Online Library for rules of use; OA articles are governed by the applicable Creative Commons License

Author Manuscript

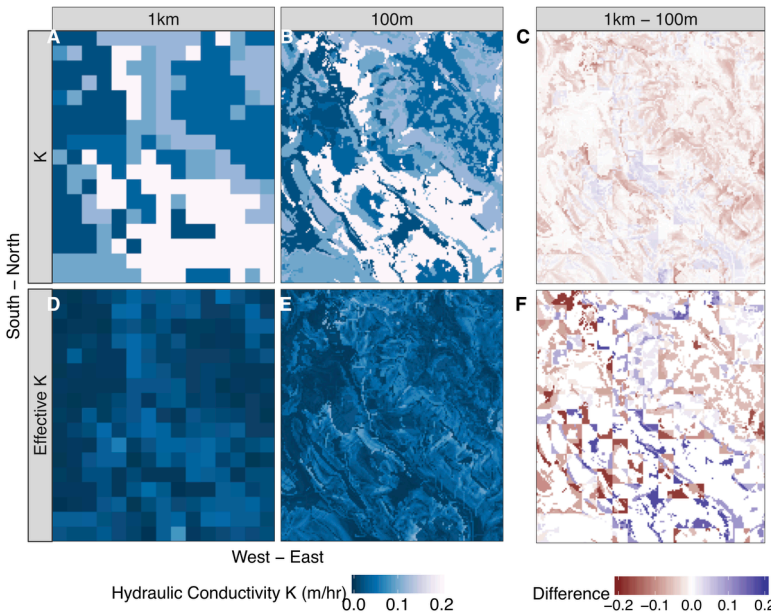

HYP_13327_F11.tiff

This article is protected by copyright. All rights reserved.

10991085, 2019, 3, Downloaded from https://onlinelibrary.wiley.com/doi/10.1002/hyp.13327, Wiley Online Library on [23/01/2023]. See the Terms and Conditions (https://onlinelibrary.wiley.com/terms-and-conditions) on Wiley Online Library for rules of use; OA articles are governed by the applicable Creative Commons License

Author Manuscript

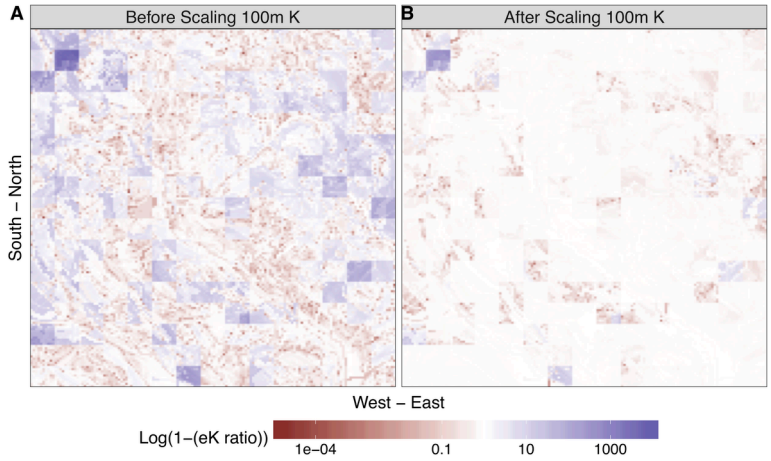

HYP_13327_F12.tiff

This article is protected by copyright. All rights reserved.

10991085, 2019, 3, Downloaded from https://onlinelibrary.wiley.com/doi/10.1002/hyp.13327, Wiley Online Library on [23/01/2023]. See the Terms and Conditions (https://onlinelibrary.wiley.com/terms-and-conditions) on Wiley Online Library for rules of use; OA articles are governed by the applicable Creative Commons License

Author Manuscript

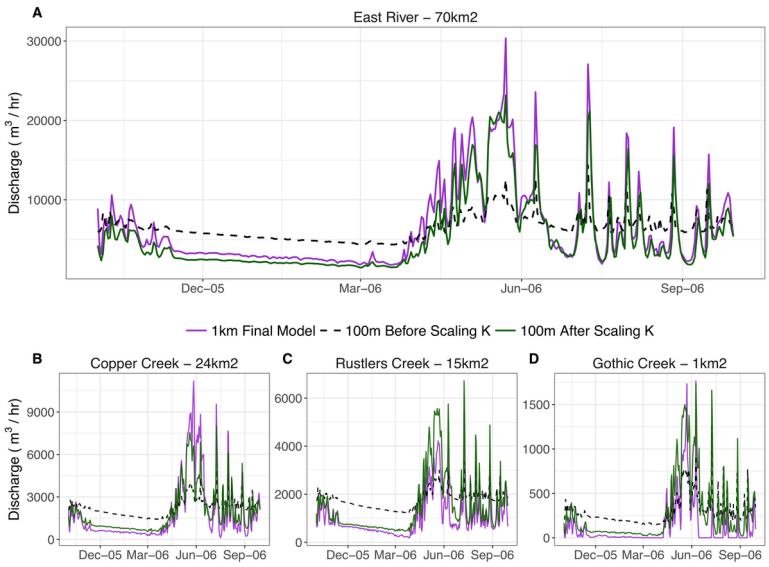

HYP_13327_F13.tiff

This article is protected by copyright. All rights reserved.

10991085, 2019, 3, Downloaded from https://onlinelibrary.wiley.com/doi/10.1002/hyp.13327, Wiley Online Library on [23/01/2023]. See the Terms and Conditions (https://onlinelibrary.wiley.com/terms-and-conditions) on Wiley Online Library for rules of use; OA articles are governed by the applicable Creative Commons License

Author Manuscript

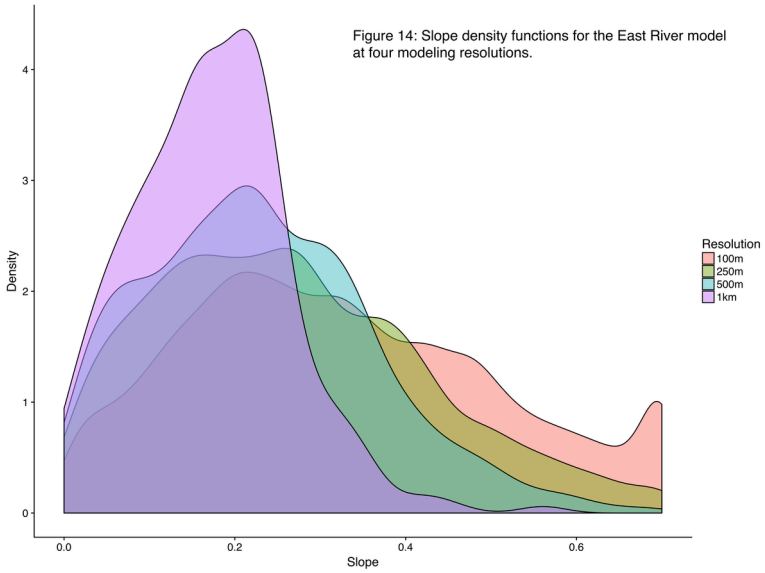

HYP_13327_F14.tiff

This article is protected by copyright. All rights reserved.

10991085, 2019, 3, Downloaded from https://onlinelibrary.wiley.com/doi/10.1002/hyp.13327, Wiley Online Library on [23/01/2023]. See the Terms and Conditions (https://onlinelibrary.wiley.com/terms-and-conditions) on Wiley Online Library for rules of use; OA articles are governed by the applicable Creative Commons License

Author Manuscript

Hydraulic Conductivity (defined by geologic or soil unit throughout domain) Scaled Over 3 Orders of Magnitude				**Mannings n parameter (originally defined by vegetation at land surface) set to constant value everywhere or variably scaled with and without stream network.**			
Conductivity Scaling Factor	Basement	Geology	Soils	Constant mannings ($m^{1/3}/s$)	Mannings Scaling Factor	Assigned n scaled	Scaled with Stream Channel Designations
0.01K	b.01K	g.01K	s.01K	cn.02 (minimum empirical estimates)	Baseline (1n)	b	bs
0.1K	b.1K	g.1K	s.1K	cn.2 (maximum empirical estimates)	10n	s10n	ss10n
Baseline (1K)	b	b	b	cn2	100n	s100n	ss100n
10K	b10K	g10K	s10K	cn20			

TABLE 1: Eighteen sensitivity experiments with Hydraulic conductivity and Manning's *n* were constructed at both 100m and 1km resolution, resulting in 36 total configurations. Layer configuration and initial parameter estimates for *K* are shown to the right.

This article is protected by copyright. All rights reserved.

10991085, 2019, 3, Downloaded from https://onlinelibrary.wiley.com/doi/10.1002/hyp.13327, Wiley Online Library on [23/01/2023]. See the Terms and Conditions (https://onlinelibrary.wiley.com/terms-and-conditions) on Wiley Online Library for rules of use; OA articles are governed by the applicable Creative Commons License

Author Manuscript

Comparison Timeseries	vs	Effective *K* Timeseries	Slope	R^2
Observed	vs	100m Baseline	0.42	0.41
Observed	vs	100m Effective *K*	1.30	0.51
1km Final Model	vs	100m Baseline	0.31	0.24
1km Final Model	vs	100m Effective *K*	0.95	0.52
1km Final Model	vs	250m Baseline	0.45	0.92
1km Final Model	vs	250m Effective *K*	1.22	0.89
1km Final Model	vs	500m	0.64	0.93
1km Final Model	vs	500m Effective *K*	1.33	0.88

TABLE 2: Slope and R^2 values for effective *K* simulations at multiple resolutions vs. observed timeseries and final 1km simulation.

This article is protected by copyright. All rights reserved.

10991085, 2019, 3, Downloaded from https://onlinelibrary.wiley.com/doi/10.1002/hyp.13327, Wiley Online Library on [23/01/2023]. See the Terms and Conditions (https://onlinelibrary.wiley.com/terms-and-conditions) on Wiley Online Library for rules of use; OA articles are governed by the applicable Creative Commons License